*Radio Science*, Volume 24, Number 1, Pages 85–98, January–February 1989

# Ionospheric incoherent scatter measurements with the middle and upper atmosphere radar: Techniques and capability

*Toru Sato,*[1] *Atsuo Ito,*[2,3] *William L. Oliver,*[1,4] *Shoichiro Fukao,*[1] *Toshitaka Tsuda,*[1] *Susumu Kato,*[1] *and Iwane Kimura*[2]

(Received February 9, 1988; revised July 27, 1988; accepted September 15, 1988.)

The MU (middle and upper atmosphere) radar of Japan is a 46.5-MHz pulse-modulated monostatic Doppler radar with an active phased array antenna which consists of 475 crossed yagis. This system has been used primarily, since its initial observations with a partial system in 1983, to observe backscatter from irregularities in the atmospheric index of refraction in the mesosphere, stratosphere, and troposphere (MST radar). However, this system was also designed to be able to observe the incoherent scattering (IS) from ionospheric plasma as well. We report here the capability of this system for IS measurements. This paper describes the observational technique employed for MU radar IS measurements, examines the expected accuracy of the plasma parameter measurements, and presents sample results to demonstrate the current capability.

## 1. INTRODUCTION

The middle and upper atmosphere (MU) radar was constructed at Shigaraki (34.85°N, 136.10°E) during 1981–1984, with observations commencing with a partial system in 1983. The basic concepts and descriptions of the completed system are described by *Fukao et al.* [1985*a*, *b*]. *Kato et al.* [1984, 1986] have described the first results obtained with this system for observing turbulence, winds, and related quantities in the middle and lower atmosphere. These reported uses have relied upon the strong coherent echo mechanisms occurring in the middle and lower atmospheric regions.

The MU radar was also designed to have a secondary capability to observe the very weak incoherent scattering originating from the free electrons in the ionosphere. This paper reports the implementation of such an ionospheric incoherent scatter (IS) radar capability with the MU radar. We begin our presentation with a description of the observational and data analysis techniques developed for IS measurements. The sensitivity of the MU radar is compared with the sensitivities of other existing IS radars. Then we discuss the accuracy of the estimated electron density, the ion and electron temperatures, and the ion drift velocity with the aid of numerical simulations. We end with a presentation of preliminary observations to demonstrate the capability of the MU radar as an IS radar. Several geophysically interesting phenomena found so far are reported elsewhere [*Oliver et al.*, 1988*a*, *b*].

## 2. SYSTEM AND OBSERVATIONAL TECHNIQUES

We refer the reader to *Kato et al.* [1984] and *Fukao et al.* [1985*a*, *b*] for a detailed description of the MU radar system. We present here a brief outline of the aspects of this system of particular pertinence to ionospheric incoherent scatter measurements.

The MU radar is a monostatic pulsed Doppler radar with an active phased array antenna operating at 46.5 MHz. The peak and average radiation powers are 1 MW and 50 kW, respectively. The basic parameters of the MU radar are given in Table 1.

The MU radar is designed to transmit a pulse as short as 1 $\mu$s. Accordingly, an exclusive bandwidth of 1.65 MHz has been assigned in Japan for MU radar operation. This pulse width affords us a height resolution of 150 m. However, a much longer pulse is usually used for ionospheric observations because of the very limited signal-to-noise ratio ($S/N$) as discussed later.

[1]Radio Atmospheric Science Center, Kyoto University, Uji, Kyoto, Japan.
[2]Department of Electrical Engineering II, Kyoto University, Kyoto, Japan.
[3]Now at NEC Corporation, Abiko-shi, Chiba, Japan.
[4]Now at Department of Electrical, Computer, and Systems Engineering, Boston University, Boston, Massachusetts.



Paper number 88RS03692
0048-6604/89/88RS-03692$08.00

TABLE 1. Basic Parameters of the MU Radar

| Parameter | Value |
|---|---|
| Location | Shigaraki, Shiga, Japan (34.85°N, 136.10°E) |
| Radar system | monostatic pulse radar; active phased array system |
| Operational frequency | 46.5 MHz |
| Antenna | circular array of 475 crossed yagis |
| Aperture | 8330 $m^2$ (103 m in diameter) |
| Beam width | 3.6° (one way; half power for full array) |
| Steerability | steering is completed in each IPP |
| Beam directions | 1657; 0°–30° off zenith angle |
| Polarizations | linear and circular |
| Transmitter | 475 solid state amplifiers (transmit/receive modules; each with output power of 2.4 kW peak and 120 W average) |
| Peak power | 1 MW (maximum) |
| Average power | 50 kW (duty ratio 5%) (maximum) |
| Bandwidth | 1.65 MHz (maximum) (pulse width: 1–512 $\mu$s variable) |
| IPP | 400 $\mu$s to 65 ms (variable) |
| Receiver | |
| Bandwidth | 1.65 MHz (maximum) |
| IF | 5 MHz |
| Analog to digital converter | 12 bits × 8 channels |
| Pulse compression | binary phase coding up to 32 elements; Barker and complementary codes presently in use |

After *Fukao et al.* [1985*a*].

Unlike the mesosphere-stratosphere-troposphere (MST) observations, which are characterized by a long signal correlation time of the order of a second, the signal correlation time of the ionospheric incoherent scattering is of the order of a millisecond, being shorter than the interpulse period (IPP). Therefore spectral estimates must be made within one IPP. Several types of IS experiments have been implemented on the MU radar according to the type of ionospheric parameter desired to observe.

A single pulse of $\sim$500 $\mu$s length, which is the longest pulse available to the MU radar, has been used for power profile measurements. Since its height resolution is a poor 75 km, pulse compression with 7-or 13-bit Barker codes is often applied, resulting in height resolutions of 10 or 6 km, respectively. It should be noted that the $S/N$ ratio for IS and MST radar measurements is inversely proportional to the number of bits used for the pulse compression under the limitation of a fixed total pulse length. This is unlike the case of the scattering from a hard target, where $S/N$ is not affected by the compression. The number of bits is determined by a compromise between required height and time resolutions. These experiments yield electron density measurements in the $E$ and $F$ regions.

Multipulse transmissions have been used for spectral measurements to observe $F$ region thermal and drift motions. These have included two-, three-, four-, and five-pulse measurements, yielding, respectively, one, three, six, and 10 lags on the autocorrelation function (ACF) of the scattered signal. The length of each transmission is again subject to the limitation that the sum of the pulse lengths during 1 IPP should not exceed 512 $\mu$s. Usually, pulse compression is not applied to these waveforms to maximize the $S/N$ ratio when the multipulse technique is used. The coded single pulses or the multipulse waveforms are designed to use most of the available 512 $\mu$s of transmission time each IPP to maximize returned signal strength. As the transmitter duty cycle is 5% maximum, we therefore use an IPP of about 10 ms.

The two-pulse experiment, measuring only one lag on the ACF, is essentially a pulse pair Doppler drift measurement as commonly used in Doppler weather radars [e.g., *Doviak and Zrnić*, 1984], allowing the ionospheric drift velocity to be obtained. The three-, four-, and five-pulse waveforms yield the additional spectral information required for temperature determination. A larger number of lags gives more information in determining the shape of the ACF, but at an expense of a poorer $S/N$. Relations between the

TABLE 2. Examples of Transmission Waveform Timing Parameters

| Timing parameter | Waveform | | | | |
|---|---|---|---|---|---|
| | 7-Bit Barker | Two Pulse | Four Pulse (*A*) | Four Pulse (*B*) | Five Pulse |
| Number of ACF lags | 1 | 1 | 6 | 6 | 10 |
| Subpulse length, $\mu$s | 64 | 256 | 96 | 128 | 64 |
| Maximum ACF lag, $\mu$s | 0 | 512 | 1152 | 1536 | 1408 |
| Length of waveform, $\mu$s | 448 | 768 | 1248 | 1664 | 1472 |
| Minimum height, km* | 78.2 | 117.8 | 198.2 | 260.5 | 231.7 |
| Measured quantities | $N_e$ | $V_d$ | $V_d$, $T_e$, $T_i$ | $V_d$, $T_e$, $T_i$ | $V_d$, $T_e$, $T_i$ |

$N_e$ is the electron density, $V_d$ is the drift velocity, $T_e$ is the electron temperature, and $T_i$ is the ion temperature.

*Values are for vertical beam. A system guard time of 74 $\mu$s has been included.

number of pulses and the expected accuracy of the spectral parameters are examined in section 4. Table 2 lists several pulse modes available with the ionospheric observations by the MU radar. Here we restrict the subpulse lengths to be multiples of 32 $\mu$s owing to some hardware limitations of the MU radar system. Among various polarizations available to the MU radar the right-hand circular polarization is used for all ionospheric observations.

In most experiments the antenna beam direction is switched alternately to the magnetic north, east, south, and west directions at 20° zenith angle at every IPP interval. This allows reconstruction of vector velocities and also allows the detection of the horizontal propagation of ionospheric phenomena between beams. Because the MU radar may change the beam direction every IPP, it can essentially observe in different directions simultaneously. This is a great advantage over large-dish antennas, which require slow mechanical motion of massive structures to change pointing direction. Such large-dish antennas may observe in different directions only sequentially, with associated time differences between observing directions and possible lost observing time during antenna transfer between observing directions.

Because of a relatively long correlation time at our frequency of 46.5 MHz, we have an intrinsic conflict between the minimum observable height $h_{\min}$ and the maximum lag $\tau_{\max}$ of the ACF. The restrictions that the sampling of the received signal can be started only after the entire train of the multipulse waveform is transmitted and that $\tau_{\max}$ is limited by the length of the train lead to a simple relation

$$h_{\min} \geq (c/2)(\tau_{\max} + nt_p + t_s) \cos \theta \quad (1)$$

where $c$ is the speed of light, $t_p$ is the subpulse length, $n$ is the number of subpulses used for the pulse compression, $\theta$ is the antenna beam zenith angle, and $t_s$ is the system guard time for switching from transmission to reception. For ionospheric observations, $t_s$ is 74 $\mu$s, and $t_p$ is chosen to be 32–512 $\mu$s. The guard time $t_s$ includes delays for the response of the transmit/receive switch and the band-limiting filter of the receiver. The narrowest bandwidth of the filter available in the MU radar system is the one matched for 32-$\mu$s pulse. Any bandwidth narrower than this is realized by using the received signal correlator for the pulse decompression as a digital low-pass filter. Since the transmit pulses are also generated in the same manner, they constitute a matched pair.

In order to derive the electron and ion temperatures from the shape of ACF, it is necessary to set $\tau_{\max}$ to be at least about 1 ms, as shown later. Therefore $h_{\min}$ cannot be made smaller than 100 km, which prevents us from observing the $E$ region by this technique at our frequency. A pulse-to-pulse correlation technique as used in MST experiments should be used for $E$ region observations. The pulse-to-pulse correlation technique, however, experiences the problem of range aliasing. If we use an IPP of about 1 ms, appropriate for $E$ region ACF definition, we experience multiple signal returns from heights separated by 150 km. Thus $F$ region signals would contaminate the $E$ region signals, and these contaminating signals would be neither small in amplitude nor greatly different in frequency characteristics to allow their neglect or spectral discrimination. It would be possible, however, to measure only the ion drift velocity using a two-pulse scheme with a small interval between pulses, which would provide useful information concerning tides and waves at $E$ region heights.

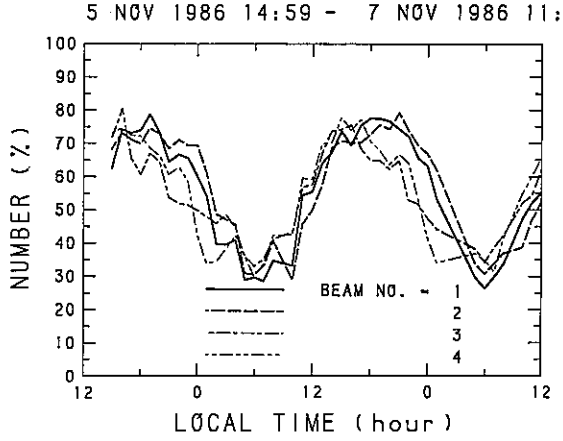


Fig. 1. Portion of collected data accepted by the meteor rejection test.

Another difficulty we have at $E$ region heights is strong echoes from meteor trails. These are specular reflections of great strength, in comparison with the wanted incoherent signal, and must be removed before summing with clean data to prevent ruinous contamination of the integrated result. However, because of the high sensitivity of the MU radar, even a very small meteor can contaminate the data, and we have not been able to develop a reliable meteor rejection algorithm for $E$ region heights. As a result, our current IS observations are limited to $F$ region heights of above around 200 km.

It should be noted that even at $F$ region heights, rejection of meteor trail echoes is important, because very strong meteor trail echoes can be received even through low-elevation sidelobes. For this case the echoes from the meteor height region 80–120 km appear at $F$ region range gates. As long as the occurrence frequency of these echoes is not too high, it is possible to reject them on the basis of the knowledge of statistical fluctuations of normal incoherent scatter echoes and meteor trail echoes.

Since the lifetime of meteor trail echoes is 0.1–1 s, the received echo power (or ACF) is first averaged over 1 s at each range gate. Then 10 of these averaged profiles are taken and stored in separate buffers. At each range gate, mean echo power $P_a$ is estimated from the observed minimum value $P_{\min}$ among the 10 data by making the following correction assuming that they follow the normal distribution:

$$P_a = P_{\min}/(1 + d \cdot \sigma_c)$$
$$d = \int_{-\infty}^{\infty} \alpha \mathscr{S}(\alpha) N_{\min} \left\{ \int_{\alpha}^{\infty} \mathscr{S}(x)\, dx \right\}^{N_{\min}-1} d\alpha \qquad (2)$$

where $\sigma_c$ is the expected ratio of the standard deviation to the mean, which is determined by the number of samples averaged in 1 s of data, $\mathscr{S}(x)$ is the normal probability distribution function, and $N_{\min}$ is the number of data used to find the minimum ($=10$).

The entire height profile is rejected when it contains one or more range gates where the echo power is larger than $P_a$ times a certain threshold factor (5–10). This is because neighboring range gates may be contaminated by the range sidelobes of the pulse compression code when a strong meteor echo appears at one range gate. The rest of the $N_{\min}$ height profiles are averaged in time to give 10 s mean data, which are recorded on magnetic tape. Figure 1 shows a plot of the portion of the collected data that were accepted by this test as a function of time for a typical experiment. The diurnal nature of the rejection simply reflects the established diurnal pattern of occurrence of meteor trails. It should be noted that this rejection scheme also removes echoes from artificial satellites and their debris, aircrafts, etc.

## 3. ESTIMATION OF ELECTRON DENSITY

The radar equation for uniformly distributed electrons gives the received signal strength as [e.g., *Evans*, 1969]

$$P_s = \frac{P_t L c \tau N_e \sigma \lambda^2}{128\pi^3 R^2} \int_{\phi} \int_{\theta} G^2(\theta, \phi) \sin\theta \, d\theta \, d\phi \quad \text{(W)} \qquad (3)$$

where $P_t$ is the transmitter power (watts), $L$ is the antenna and cable loss factor, $\tau$ is the pulse length (seconds), $N_e$ is the electron density ($m^{-3}$), $\sigma$ is the scattering cross section per electron (meters squared), $\lambda$ is the radar wavelength (meters), $R$ is the range from radar to scattering volume (meters), and $G(\theta, \phi)$ is the antenna gain at zenith angle $\theta$ and azimuth $\phi$.

Since the MU radar antenna has a circular array with a uniform excitation, (3) reduces to

$$P_s = \frac{0.88 P_t L c \tau A N_e \sigma}{16\pi R^2} \quad \text{(W)} \qquad (4)$$

where $A$ is the effective collecting area of the antenna. The constant 0.88 in this equation is a factor resulting from the integration of the gain over the antenna beam shape; this factor would be unity if the beam were uniform over the half-power beam width and zero outside. *Evans* [1969] has given a value of 0.76 for a typical parabolic antenna.

The collective plasma scattering cross section per electron $\sigma$ is a function of the ratio $T_r$ of the electron

and ion temperatures [*Buneman*, 1962]:

$$\sigma = \sigma_e/(1 + T_r) \quad (m^2) \tag{5}$$

where $\sigma_e$ is the scattering cross section of an independent electron ($0.998 \times 10^{-28}$ m$^2$).

If the system constants in (4) are known precisely, it is possible to estimate $N_e/(1 + T_r)$ directly from $P_s$. However, this is not the case for the MU radar, where the absolute receiver gain is hard to calibrate because of the distributed transmitter/receiver system configuration, which, in turn, makes it difficult to measure the absolute scattered power $P_s$. Instead, a lumped system constant is determined by comparing the echo power obtained from the peak of the $F$ layer during nighttime (when we may assume $T_r = 1$), with the $f_0F_2$ data obtained by an ionosonde located on the MU observatory site:

$$C = P_{max}/N_{max} \qquad (T_r = 1) \tag{6}$$

where $P_{max}$ and $N_{max}$ are $P_s$ and $N_e$ evaluated at the $F$ layer peak. A mean of the $C$ values obtained throughout the night is then used as a single lumped system constant for interpretation of all power data. Equation (4) then reduces to

$$P_s = \frac{CR_{max}^2}{(1 + T_r)R^2} N_e \tag{7}$$

where $R_{max}$ is the height of $F$ layer peak. Then using echo power and ionosonde data during daytime, we can estimate the value of $T_r$ at the $F$ layer peak. Figure 2 shows a diurnal variation of $T_r$ at the $F_2$ peak height obtained by (7). Arrows indicate the sunrise and sunset times at 250 km altitude. The reasonable diurnal variation of $T_r$ suggests the stability of the system parameters.

As far as the MU radar is concerned, all system constants appearing in (4) except the receiver gain can safely be assumed to be stable owing to the solid state architecture of the system, which has been confirmed by periodic maintenance tests. If we assume that the only variable is the receiver gain, we can calibrate it by using the background noise level. The received noise power is given by

$$P_n = kT_{sys}B \quad (W) \tag{8}$$

where $k$ is Boltzmann's constant ($1.38 \times 10^{-23}$ joules/kelvin) $T_{sys} = T_n + T_{rec}$ is the system noise temperature (kelvins), $T_n$ is the background noise temperature (kelvins), $T_{rec}$ is the receiver and line loss temperature (kelvins), and $B$ is the receiver bandwidth (hertz).

At 46.5 MHz, $T_n$ dominates over $T_{rec}$, which has been measured to be constant at 2000 K. The system constant $C$ in (7) determined as above can also be used to calibrate $T_n$. $T_n$ is estimated by the mean received power at ranges beyond 700 km, where echoes from the plasma are negligible. In order to obtain a sufficient number of samples for noise estimation, the echo power is usually measured up to 1300 km range. The obtained diurnal variation of $T_n$ shows good consistency with that extrapolated from measurements at higher frequencies [e.g., *Kraus*, 1966], varying between 5000 K and 16,000 K depending on the celestial time of day. After establishing the diurnal variation model of $T_n$ by accumulating a large number of data, it will become possible to calibrate $P_s$ on the basis of the measured $P_n$ and the model, although this is yet to be done.

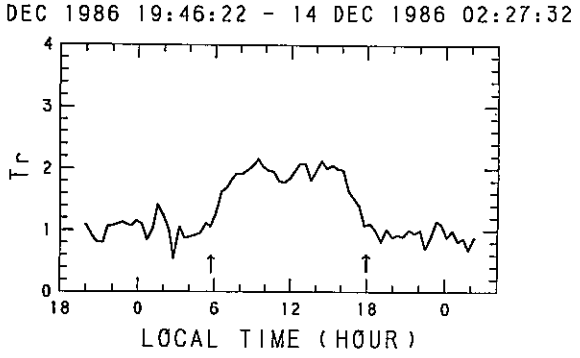


Fig. 2. Diurnal variation of $T_r (= T_e/T_i)$ at $F_2$ peak height.

We wish now to compare the sensitivity of the MU radar for incoherent scatter observations with that of the other existing IS radars. We will investigate the signal-to-noise ratio ($S/N$), which is the critical factor for the MU radar IS observations, based on (4) and (8). For our comparison we will make calculations of $S/N$ for the case of an electron density $N_e$ of $10^{12}$ m$^{-3}$ at a range $R$ of 300 km using a pulse length $T$ of 500 $\mu$s. A loss factor of 0.75, applicable to the MU radar, is used for all radars, although it may be an overestimate within a factor of 2 or so for some of those radars. Use of different values of $L$ would change the $S/N$ values derived below, but it will not affect the discussion here. It would be worth mentioning that the effective area $A$ of the MU radar antenna is very close to the physical area because of the uniform excitation of the array and the optimum design of the array element.

We must choose a receiver bandwidth $B$ wide enough to enclose the spectral width of the received signal. Signal spectral broadening is caused by two effects: (1) the spectrum of the pulse waveform, and

TABLE 3. Comparison of the MU Radar Sensitivity With Other Existing IS Radars

| IS Facility | Frequency, MHz | $P_t$, MW | | $A$, m$^2$ | $T_{sys}$, K | $B$, kHz | $S/N$ |
|---|---|---|---|---|---|---|---|
| | | Peak | Average | | | | |
| Jicamarca | 49.9 | 6.0 | 0.4 | 71,900 | 10,000 | 2.4 | 1400 |
| Arecibo | 430 | 2.0 | 0.1 | 45,500 | 150 | 23.4 | 2000 |
| Millstone Hill A | 440 | 5.0 | 0.25 | 2,334 | 150 | 24.0 | 260 |
| Millstone Hill B | 440 | 5.0 | 0.25 | 930 | 150 | 24.0 | 100 |
| Millstone Hill C | 1295 | 2.5 | 0.125 | 190 | 150 | 70.4 | 4 |
| Sondrestrom | 1290 | 5.0 | 0.12 | 400 | 100 | 70.4 | 22 |
| European Incoherent Scatter (EISCAT) A | 933 | 1.5 | 0.1875 | 520 | 115 | 50.8 | 11 |
| EISCAT B | 933 | 1.5 | 0.1875 | 520 | 40 | 50.8 | 30 |
| EISCAT C | 224 | 2.0 | 0.25 | 3,250 | 220 | 12.2 | 190 |
| Altair A | 415 | 20.0 | 0.112 | 722 | 785 | 22.6 | 64 |
| Altair B | 155.5 | 10.0 | 0.112 | 820 | 992 | 8.4 | 78 |
| MU | 46.5 | 1.0 | 0.05 | 8,330 | 10,000 | 2.4 | 27 |

Note: Not all of the radars listed above normally operate, nor in some cases are they able to opeate, with the listed parameters. Nevertheless, the above comparison should give an adequate idea of the relative potential sensitivities of these radars for long-pulse power measurements.

(2) the Doppler broadening caused by the thermal motions of the scattering medium. To match our assumed 500-$\mu$s pulse, we need a filter width of 2 kHz. The spectral broadening caused by the thermal motions is about 4 times the Doppler shift caused by an ion approaching the radar at mean thermal speed [*Evans*, 1969],

$$B = \frac{4f}{c}\left(\frac{8kT_i}{m_i}\right)^{1/2} \tag{9}$$

where $f$ is the radar operating frequency and $T_i$ and $m_i$ are the temperature and mass of the ion, respectively. For the predominant $O^+$ ion of the $F$ region at a typical temperature $T_i = 1000$ K,

$$B = 2.72 \times 10^{-5} f \tag{10}$$

This bandwidth is larger than the waveform spectral broadening of 2 kHz for a frequency higher than 75 MHz. Thus we use (10) for all radars except the MU and Jicamarca radars. Since the thermal broadening adds to the pulse broadening in an rms sense, the total bandwidth at 50 MHz becomes 2.5 kHz.

By combining (4) and (8) with the above values for $L$ and $\tau$ and assuming $T_r = 1$, the $S/N$ formula is obtained as

$$S/N = \frac{0.079 P_t A}{B T_{sys}} \tag{11}$$

Table 3 lists the pertinent parameters for each facility and the $S/N$ computed from (11). These $S/N$ values give the potential maximum and may not represent typical values achieved by these facilities, because wider bandwidths are generally used to allow larger Doppler velocities and also because the antenna efficiency may be lower than assumed here.

On a relative $S/N$ basis we can see from this table that the Mu radar falls in a category of least sensitive IS radars. On an absolute $S/N$ basis, however, Table 3 shows that all of the listed facilities are highly capable of making the assumed incoherent scatter measurement for the assumed ionospheric condition. Actually, what is important in the data analysis is not the $S/N$ itself, but the relative uncertainty in the signal. This factor, often referred to as the signal detectability [*Gage and Balsley*, 1978], is defined, after modifying to include the effect of the signal fluctuation, as

$$D \equiv \frac{P_{s0}}{(\Delta P_{s0}^2 + \Delta P_{n0}^2)^{1/2}} = \frac{1}{1 + B_r N/S}\sqrt{M} \tag{12}$$

where $P_{s0}$ is the peak spectral density of the signal, $P_{n0}$ is the average spectral density of the noise, $\Delta P_{s0}$ and $\Delta P_{n0}$ are standard deviations of $P_{s0}$ and $P_{n0}$, respectively, $B_r$ is the spectral width of the signal relative to the receiver bandwidth, and $M$ is the number of independent samples used in the averaging process. The receiver bandwidth is usually chosen so that $B_r \lesssim 1$. We can see that the detectability does not improve greatly as $S/N$ increases above unity. In this sense all of the radars listed in Table 3 are

equally capable of making the desired ionospheric backscattered power measurement. We should note, however, that for poorer $S/N$ conditions than considered here, we have to sacrifice time and/or height resolution with the MU radar observations in order to obtain the same $D$ as other powerful IS radars.

## 4. ESTIMATION OF TEMPERATURE AND VELOCITY

The thermal and mean motions of the ions and electrons affect the shape of the backscattered echo power spectrum and, equivalently, the ACF as follows for the $F$ region observations:

$$\rho(\tau) = P_s \rho_0(\tau; T_r, T_i, q) \exp\left(-j \frac{4\pi}{\lambda} V_d \tau\right) \tag{13}$$

where $\rho_0$ is the normalized ACF without mean motion, $\tau$ is the time lag, $q = [O^+]/N_e$, $N_e = [O^+] + [NO^+] + [O_2^+]$, and $V_d$ is the mean ion Doppler velocity.

These effects have been thoroughly studied theoretically, and expressions for the function shape of $\rho_0$ have been given [e.g., *Fejer*, 1961]. Therefore observed ACFs can be compared with theoretical ones in a nonlinear least squares fitting manner to give the best fit parameters. Unfortunately, however, the effect of $q$ on the ACF cannot be easily distinguished from that of $T_r$ and $T_i$, because the relative masses of $O^+$, $NO^+$, and $O_2^+$ ions are too close to give a unique feature to the ACF as $q$ is varied [*Petit*, 1968]. Thus only $P_s$, $T_r$, and $T_i$ are determined by fitting model functions $\rho_0$ to observed ones, assuming a model height profile of $q$ [*Oliver and Bowhill*, 1974]. $V_d$ can be estimated separately by fitting a straight line to the phase of observed ACF.

As mentioned above, the accuracy of estimates largely depends on the way the ACF is measured. Here we consider the effect of different multipulse observations on the accuracy of the obtained parameters via a numerical simulation in order to find the optimum pulse scheme.

We first examine the temperature estimation. Among the pulse modes listed in Table 2, the single- and two-pulse modes do not give temperature information. We also found that the parameters estimated by the three-pulse mode are too sensitive to statistical fluctuations in ACF. This is possibly because the three-pulse method gives only three lags in ACF, which has no redundancy in fitting. Also, the three lags do not necessarily fall on the ACF where the useful information lies. Therefore we restrict our discussion to four- and five-pulse modes. The use of a larger number of pulses is ruled out, as we discuss later.

As we have seen, the maximum observable lag $\tau_{max}$ of the ACF is limited by the minimum observable height $h_{min}$ by (1). We use the four-pulse ($A$) mode in Table 2 as a reference for which $h_{min} = 198.2$ km and $\tau_{max} = 1152$ $\mu$s. We compare the accuracy of the parameters estimated by this mode with those by the five-pulse mode with a slightly larger $\tau_{max}$ as shown in Table 2. The five-pulse mode provides more points on the ACF at the expense of a poorer $S/N$ because of shorter individual pulses. In order to see the merit of increasing $\tau_{max}$ by increasing the individual pulse length, we also examine the four-pulse ($B$) mode with $h_{min} = 260.5$ km and $\tau_{max} = 1536$ $\mu$s. Figure 3 shows an example of the theoretical ACF generated for $T_i = 700$ K, $T_r = 2$, and $V_d = 50$ m/s. Lags to be measured by the ($a$) four-pulse ($A$), ($b$) five-pulse, and ($c$) four-pulse ($B$) modes are indicated by circles. Note that the vertical scales are magnified for the imaginary part of ACFs.

The procedure of the computer simulation is as follows. We first generate a theoretical ACF for a given $T_r$, $T_i$, $V_d$, and $q$ at each lag. Next we add a noise ACF, which consists of an impulse at zero lag (not used in fitting) and random values with zero mean at other lags. The magnitude of these random fluctuations is determined by the $S/N$ and the number of incoherent integrations, which we choose as 200,000. The resulting time resolution is variable, because it also depends on the IPP and the number of beam directions switched alternately from one pulse to the next, but 200,000 times of integration roughly corresponds to a time resolution of 1 hour. Then we fit theoretical ACFs by a nonlinear least squares fitting algorithm to retrieve $T_r$ and $T_i$. The simulation is repeated 100 times for the same temperature situation but with different random numbers to obtain meaningful statistics.

Before comparing different pulse modes, we first examine the nature of errors. Since no appreciable bias was found in the parameter estimates, we can express the errors simply by the standard deviation of the estimates around the model value. Figure 4 shows the error in $T_i$ and $T_r$ for the four-pulse ($A$) mode versus $S/N$ ratio. The error in $T_e (= T_i T_r)$ is also shown. The three lines in each panel correspond to different model values of $T_i$. The error bars indicate the fluctuations in 100 simulations. It should be noted that although simulations are made up to positive decibel $S/N$ values to ensure fitting convergence

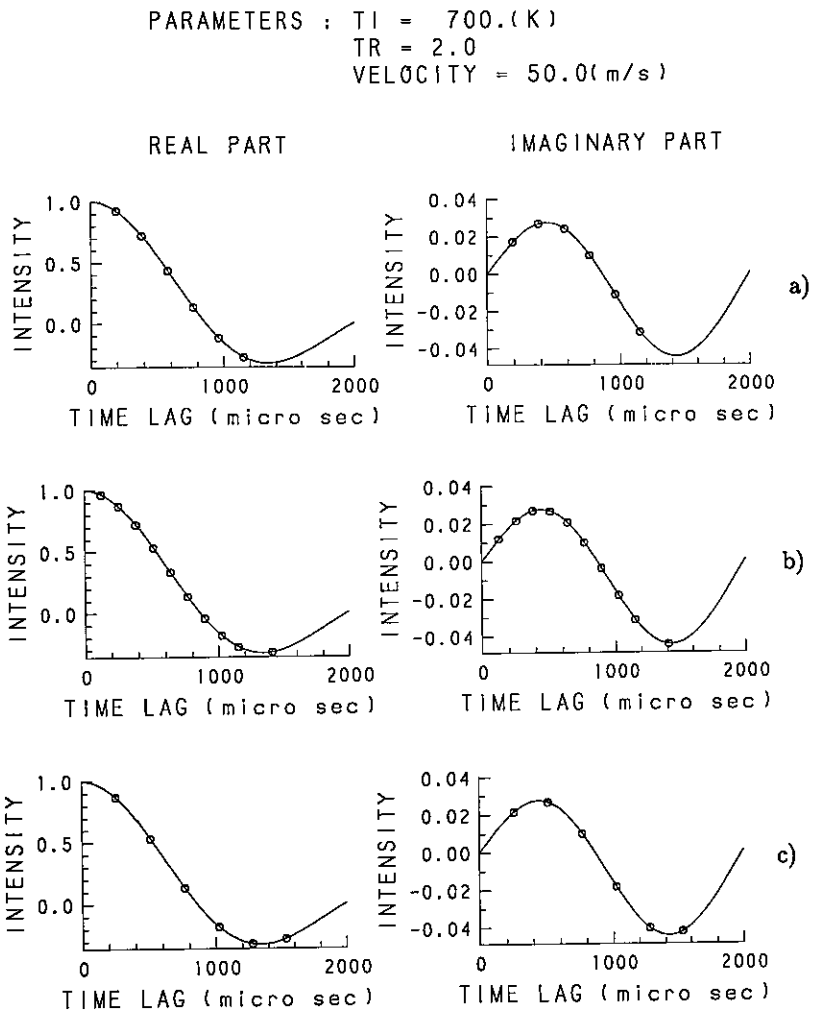


Fig. 3. Example of the theoretical ACF generated for $T_i = 700$ K, $T_r = 2$, and $V_d = 50$ m/s. Circles denote time lags to be measured by the (*a*) four-pulse (*A*), (*b*) five-pulse, and (*c*) four-pulse (*B*) modes.

for noiseless data, such positive decibel $S/N$ values cannot be encountered in real observations due to "self clutter," no matter how strong the echoes are. The self clutter is uncorrelated echoes from different heights due to the multipulse waveform [*Farley*, 1972]. It is collectively stronger than the desired echo for multipulse mode with more than two pulses. For the case of uniform echo power distribution with height, the upper limit of $S/N$ is $-4.8$ dB for the four-pulse mode and $-6$ dB for the five-pulse mode. (These conclusions are somewhat modified but basically remain valid when we consider that the different pulses may contribute somewhat different echo powers).

It is shown in Figure 4 that errors become smaller as $T_i$ increases. This is because increasing $T_i$ corresponds to increasing the maximum lag of ACF, giving a better frequency resolution in the power spectrum. An error of 10–20% is expected for $T_i$ estimates at $-10$-dB $S/N$ ratio, 20–30% for $T_r$, and 5–10% for $T_e$. It is interesting that $T_e$, which is obtained indirectly from $T_i$ and $T_r$, has better accuracy than the others. This suggests that the effects of random errors in the ACF are anticorrelated in their effects upon $T_i$ and $T_r$ determination. Figure 5 presents the same result but for a model $T_r$ of 3. Here the errors in $T_i$ are almost the same as in Figure 4, but they are significantly smaller for $T_r$. This is because

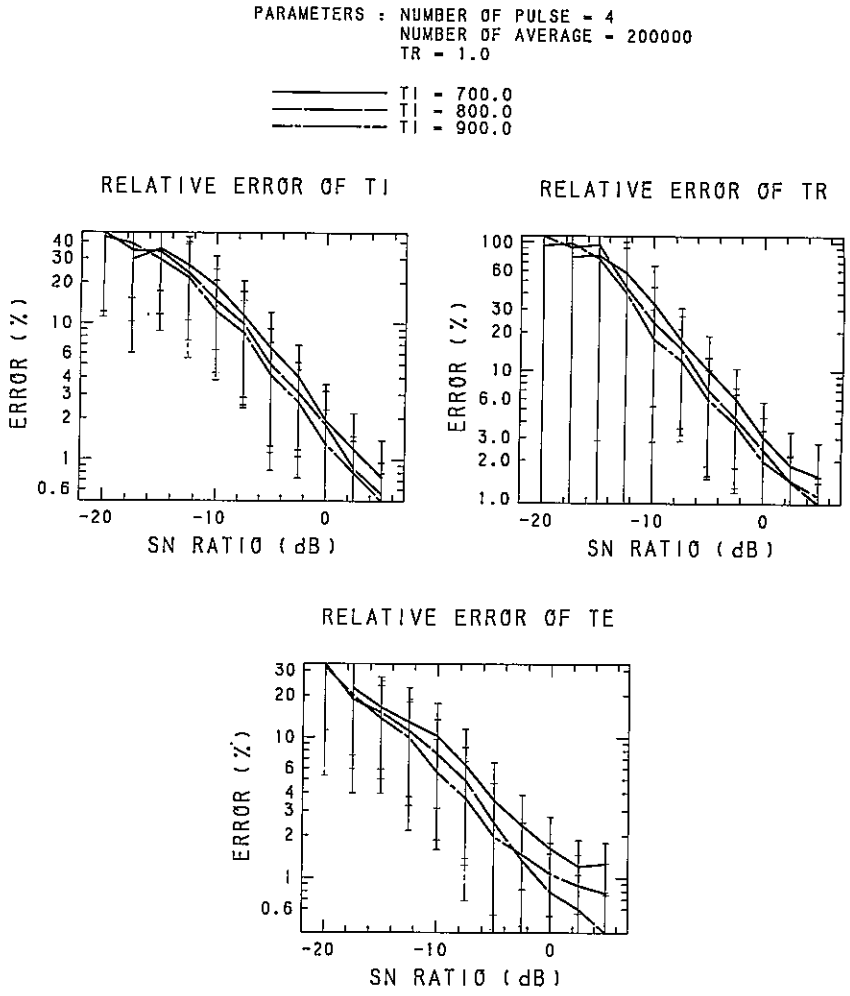


Fig. 4. Error in $T_i$, $T_r$, and $T_e$ expected for the four-pulse ($A$) mode versus $S/N$ ratio estimated by the numerical simulation. The model ACFs are generated for $T_i = 700$, 800, and 900 K, and for $T_r = 1$.

an increase in $T_r$ enhances the oscillatory nature of ACF, thus making ACF more sensitive to a small change in $T_r$, but not in $T_i$.

Figure 6 shows the accuracy of the five-pulse mode for the same situation as in Figure 4. $S/N$ in the abscissa is expressed in terms of $S/N$ for the case of the four-pulse ($A$) mode for comparison. The real $S/N$ ratio for the five-pulse mode is about 3.5 dB worse for a poor $S/N$ case because of shorter individual pulses and about 1.2 dB worse for a good $S/N$ case because of stronger self clutter. This convention for expressing $S/N$ is used throughout the figures in this section. The errors in the five-pulse mode are more than twice those in the four-pulse ($A$) mode in spite of a slightly larger $\tau_{max}$. It is clear from this comparison that increasing the number of lags in the ACF to more than six is not worthwhile when the summed length of the pulses is fixed.

On the contrary, the accuracy of the four-pulse ($B$) mode shown in Figure 7, in which the length of the individual pulses is 33% longer than the four-pulse ($A$) mode, is about 5 times better than in Figure 4. This improvement is equivalent to an enhancement in $S/N$ by about 6 dB in Figure 4, although the actual improvement in $S/N$ by making the pulse 33% longer is only 2.5 dB. This fact well demonstrates the nonlinear nature of the fitting. In reality, however, the higher $h_{min}$ of 260.7 km associated with the four-

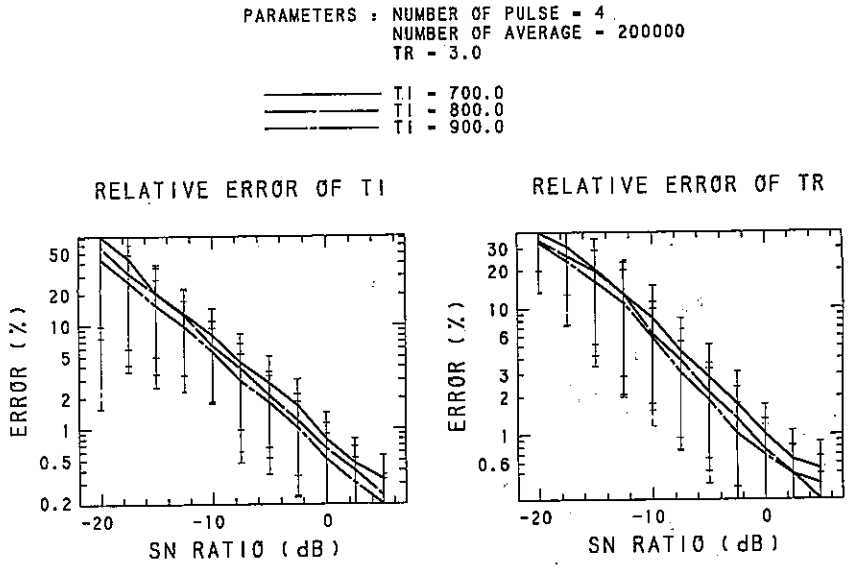


Fig. 5. Error in $T_i$ and $T_r$ under the same condition as for Figure 4, except that $T_r = 3$.

pulse ($B$) mode limits its use to only upper $F$ region observations.

Next, we examine the accuracy of the ion drift velocity estimates. Since the only parameter derived from the imaginary part of ACF is $V_d$, the least number of pulses capable of estimating $V_d$ is 2. As shown in Figure 3, the amplitude of the imaginary part of the ACF is about 2 orders of magnitude smaller than that of the real part, because the mean line-of-sight ion velocity is much smaller than the mean thermal velocity of ions.

This small amplitude results in a much larger relative error in the estimates of $V_d$ than in temperatures. Figure 8 shows the expected error in $V_d$ estimates for the four-pulse ($A$) mode. The model ACF assumes a velocity of 50 m/s, which is a typical value for $F$ region line-of-sight ion velocity. The error amounts to 60–70%, or 30–35 m/s, for the −10-dB $S/N$ ratio,

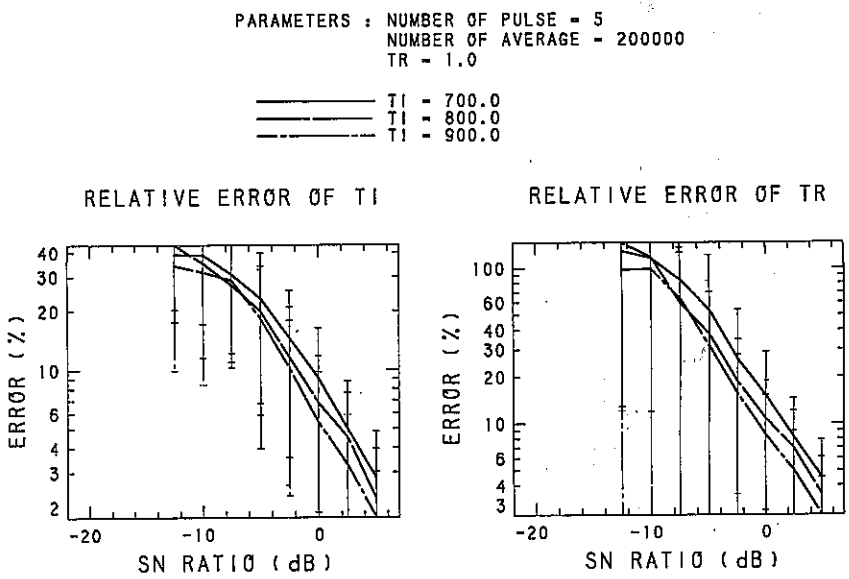


Fig. 6. Error in $T_i$ and $T_r$ under the same condition as for Figure 4, except that this is for the five-pulse mode.

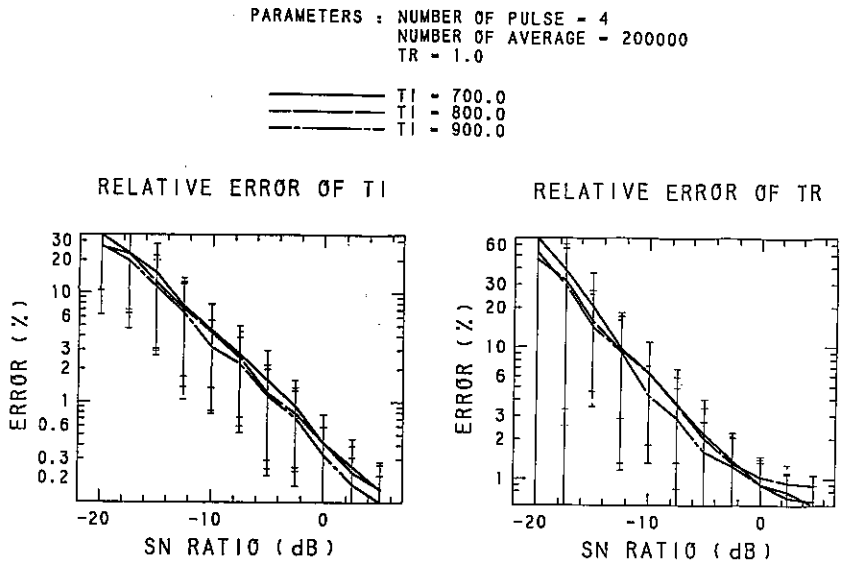


Fig. 7. Error in $T_i$ and $T_r$ under the same condition as for Figure 4, except that this is for the four-pulse ($B$) mode.

indicating that an integration time of 1 hour is far from sufficient for this mode. In order to obtain an accuracy of 10 m/s, an unrealistic integration time of 10 hours is required. Figure 9 shows the error for the same situation as in Figure 8, but with the two-pulse mode in Table 2. This mode, which makes use of the longest pulse available, gives an accuracy of 10–20% (5–10 m/s) at an expense of no temperature or density information, and also with a height resolution of 40 km. It seems essential to interlace this mode into the sequence of observations when the velocity information is required.

In summary, the four-pulse ($A$) mode will be most appropriate for a standard temperature observation.

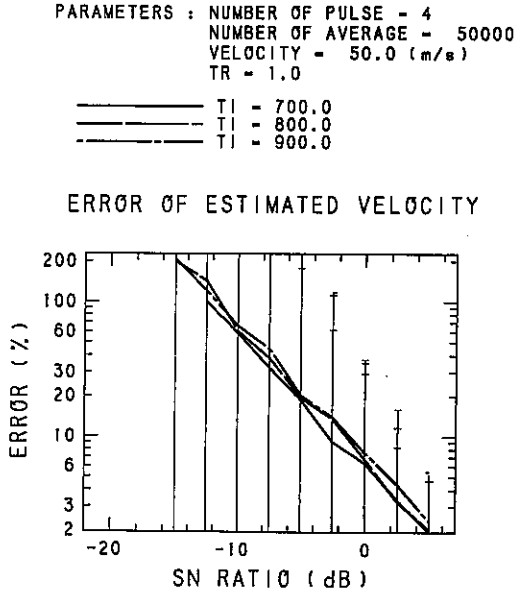


Fig. 8. Error in $V_d$ expected for the four-pulse ($A$) mode versus $S/N$ ratio estimated by the numerical simulation.

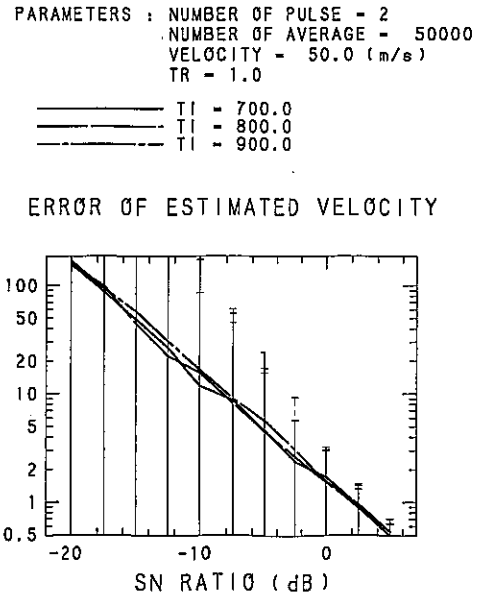


Fig. 9. Same as Figure 8, but for the two-pulse mode.

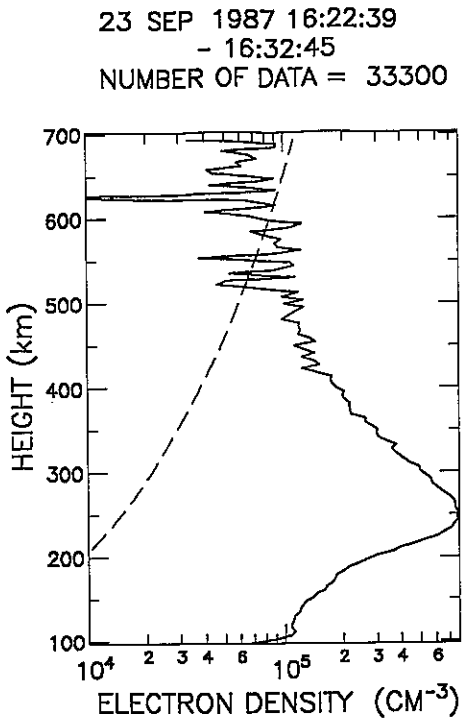


Fig. 10. An example of the electron density profile averaged for 10 min. The dashed line indicates the detectability threshold of $D = 3$.

If the limitation of a higher $h_{min}$ can be accepted, a longer individual pulse length as in the four-pulse ($B$) mode is beneficial. The use of the five-pulse mode does not seem to have any advantage for the situations considered. The only pulse mode which gives a good estimate of the ion drift velocity with an acceptable time resolution is the two-pulse mode.

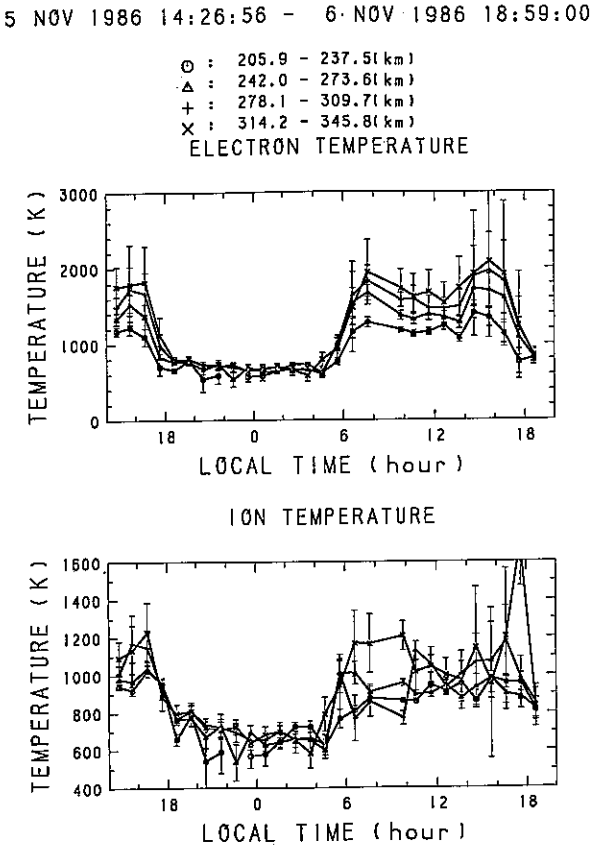


Fig. 12. Temporal variations of $T_i$ and $T_e$ for four altitudes with 32-km height resolution. Error bars indicate the accuracy expected from the numerical simulation.

## 5. SAMPLE RESULTS

Here we present some preliminary observational results obtained by the MU radar incoherent scatter measurements in order to demonstrate its current ca-

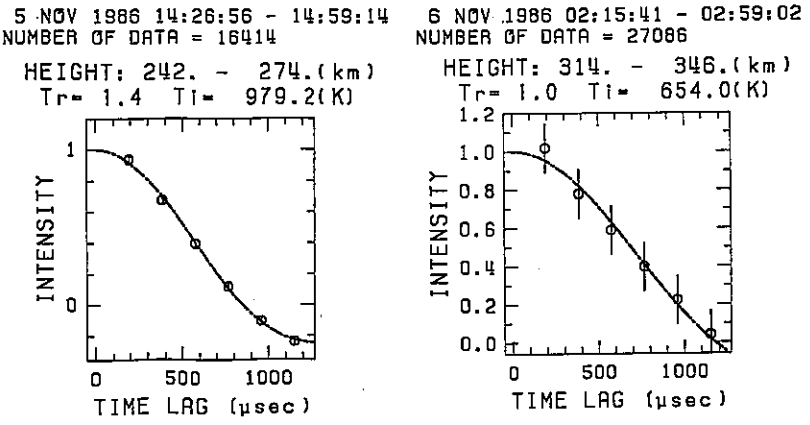


Fig. 11. Examples of daytime (left) and nighttime (right) ACFs measured with the four-pulse ($A$) mode. Circles and error bars show the 45-min mean observed ACF points and their standard deviations, respectively. The dash-dotted lines show the best fit theoretical ACFs.

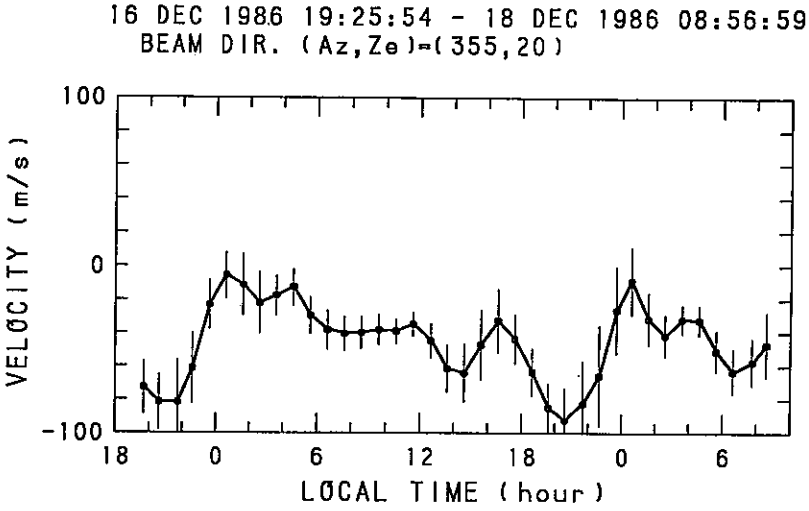


Fig. 13. Temporal variation of the line-of-sight velocity measured with the two-pulse mode. Data are averaged over the 217- to 303-km height range.

pability. Geophysically interesting results obtained so far are reported elsewhere [*Oliver et al.*, 1988*a*, *b*].

Figure 10 shows an example of the electron density profile averaged for 10 min. This measurement employed the 7-bit Barker waveform of Table 2 and an IPP of 10 ms. It is normalized by the $f_oF_2$ value measured by the on-site ionosonde. The dashed line indicates the detectability threshold of $D = 3$ in (12). Note that the maximum observable height varies not only with the electron density itself, but also with the background noise temperature, which has a diurnal variation of about 5 dB. This figure corresponds to a medium level of the background temperature.

Two examples of ACF measurements with the four-pulse (*A*) mode are shown in Figure 11. Circles and error bars show the 45-min mean observed ACF points and their standard deviations, respectively, and the dash-dotted lines show the best fit theoretical ACFs. Observed ACFs are also averaged over a 32-km height range. In calculating theoretical ACFs, only the ion component with a single constituent ($O^+$) is used. The left and right panels are typical examples of the daytime and the nighttime ACFs, respectively. It should be noted that the first lag of the measured ACF is slightly raised owing to small contamination by correlated background noise. This correlation is a consequence of the receiver band limitation. The first lag is given a weight of half of that for other lags in the fitting procedure at the moment, although it would be possible to evaluate the contamination from noise ACFs at high range gates to subtract its effect.

Temporal variations of $T_i$ and $T_e$ are drawn for four altitudes in Figure 12. This measurement employed the four-pulse (*A*) mode with an IPP of 10 ms. Individual symbols represent these parameters estimated from ACFs averaged over 32 km in height and 45 min in time. The error bars indicate the accuracy expected from the simulation in the previous section. Note that the stability of each line in the $T_e$ curves seem to suggest better accuracy in $T_e$ than in $T_i$, as predicted by the simulation.

Figure 13 shows an example of the line-of-sight ion drift velocity versus time measured with the two-pulse mode. A systematic bias of about $-23$ m/s has been detected by laboratory tests of the transmitter modules. This bias arises from a phase change of the power amplifier between the two pulses during the transmission. This value, although it needs to be monitored for a longer period and is not subtracted here, shall be corrected for in future analyses.

## 6. SUMMARY

The MU radar, constructed with a primary purpose of observing the strong backscatter from irregularity structures in the middle atmosphere, also has a demonstrated capability to detect the incoherent scatter from free electrons in the ionosphere. Incoherent scatter $S/N$ ratios in excess of 10 are attainable with long-pulse (500 $\mu$s) and matched receiver bandwidth operations. Practical spectral measurements, however, often experience $S/N$ ratios of only a few percent, and hence long integration times are

generally required to obtain geophysically useful results.

Numerical simulations have shown that the error in the ion and electron temperatures is expected to be 5–20% with the standard four-pulse experiments and with 1 hour of integration. Ion drift velocity measurements require the implementation of a separate two-pulse technique, which gives a 5–10 m/s accuracy with 1-hour resolution. Sample results have exhibited the designed capability of the MU radar as an IS radar, and expectations indicated by numerical simulations have been confirmed.

## REFERENCES

Buneman, O., Scattering of radiation by the fluctuations in a non-equilibrium plasma, *J. Geophys. Res.*, *67*, 2050–2053, 1962.

Doviak, R. J., and D. S. Zrnić, *Doppler Radar and Weather Observations*, chap. 6, Academic, San Diego, Calif., 1984.

Evans, J. V., Theory and practice of ionosphere study by Thomson scatter radar, *Proc. IEEE*, *57*, 496–530, 1969.

Farley, D. T., Multipulse incoherent scatter correlation function measurements, *Radio Sci.*, *7*, 661–666, 1972.

Fejer, J. A., Scattering of radio waves by an ionized gas in thermal equilibrium in the presence of a uniform magnetic field, *Can. J. Phys.*, *39*, 716–740, 1961.

Fukao, S., T. Sato, T. Tsuda, S. Kato, K. Wakasugi, and T. Makihira, The MU radar with an active phased array system, 1, Antenna and power amplifiers, *Radio Sci.*, *20*, 1155–1168, 1985*a*.

Fukao, S., T. Tsuda, T. Sato, S. Kato, K. Wakasugi, and T. Makihira, The MU radar with an active phased array system, 2, In-house equipment, *Radio Sci.*, *20*, 1169–1176, 1985*b*.

Gage, K. S., and B. B. Balsley, Doppler radar probing of the clear atmosphere, *Bull. Am. Meteorol. Soc.*, *59*, 1074–1093, 1978.

Kato, S., T. Ogawa, T. Tsuda, T. Sato, I. Kimura, and S. Fukao, The middle and upper atmosphere radar: First results using a partial system, *Radio Sci.*, *19*, 1475–1484, 1984.

Kato, S., T. Tsuda, M. Yamamoto, T. Sato, and S. Fukao, First results obtained with a middle and upper atmosphere (MU) radar, *J. Atmos. Terr. Phys.*, *48*, 1259–1267, 1986.

Kraus, J. D., *Radio Astronomy*, chap. 8, McGraw-Hill, New York, 1966.

Oliver, W. L., and S. A. Bowhill, The $F_1$ region during a solar eclipse, *Radio Sci.*, *9*, 189–195, 1974.

Oliver, W. L., S. Fukao, T. Sato, T. Tsuda, S. Kato, I. Kimura, A. Ito, T. Saryo, and T. Araki, Ionospheric incoherent scatter measurements with the middle and upper atmosphere radar: Observations during the large magnetic storm of February 6–8, 1986, *J. Geophys. Res.*, *93*, 14,649–14,655, 1988*a*.

Oliver, W. L., S. Fukao, T. Sato, T. Tsuda, S. Kato, I. Kimura, A. Ito, T. Saryo, and T. Araki, Ionospheric incoherent scatter measurements with the MU radar: Observations of *F*-region electrodynamics, *J. Geomagn. Geoelectr.*, in press, 1988*b*.

Petit, M., Mesures de températures, de densité électronique et de composition ionique dans l'ionosphère par diffusion de Thomson: Étude déséquilibre thermodynamique dans l'ionosphère diurne, *Ann. Geophys.*, *24*, 1–38, 1968.

---

S. Fukao, S. Kato, T. Sato, and T. Tsuda, Radio Atmospheric Science Center, Kyoto University, Uji, Kyoto 611, Japan.

A. Ito, NEC Corporation, 1131 Hinode, Abiko-shi, Chiba 270-11, Japan.

I. Kimura, Department of Electrical Engineering II, Kyoto University, Kyoto 606, Japan.

W. L. Oliver, Department of Electrical, Computer, and Systems Engineering, Boston University, Boston, MA 02215.